Chapter 10
Effect of Vascularization on Glioma Tumor Growth

Haralambos Hatzikirou, Arnaud Chauvière, John Lowengrub, J. De Groot, and Vittorio Cristini

1 Introduction

Cancer describes a group of genetic and epigenetic diseases, characterized by uncontrolled proliferation of cells, leading to a variety of pathological consequences and frequently death. Cancer progression can be depicted as a sequence of traits or phenotypes that cells have to acquire if a neoplasm (benign tumor) is to become an invasive and malignant cancer. A phenotype refers to any kind of observed morphology, function or behavior of a living cell. Hanahan and Weinberg (2000) have identified six cancer cell phenotypes: unlimited proliferative potential, environmental independence for growth, evasion of apoptosis, angiogenesis, invasion, and metastasis. The attempt to define a temporal order of tumor cells acquiring new capabilities remains still unclear in general.

H. Hatzikirou • A. Chauvière
Department of Pathology, University of New Mexico, 1 University of New Mexico, Albuquerque, NM 87131, USA
e-mail: hhatzikirou@salud.unm.edu; achauviere@salud.unm.edu

J. Lowengrub
Department of Mathematics, The University of California at Irvine, Irvine, CA, USA
e-mail: lowengrb@math.uci.edu

J. De Groot
Department of Neuro-Oncology, Cancer Medicine, The University of Texas M. D. Anderson Cancer Center, Houston, TX, USA
e-mail: jdegroot@mdanderson.org

V. Cristini (✉)
Department of Pathology and Department of Chemical and Biomedical, Engineering University of New Mexico, 1 University of New Mexico, Albuquerque, NM 87131, USA
e-mail: vcristini@salud.unm.edu

T.L. Jackson (ed.), *Modeling Tumor Vasculature: Molecular, Cellular, and Tissue Level Aspects and Implications*, DOI 10.1007/978-1-4614-0052-3_10,

In this chapter, we aim at understanding how neovascularization is coupled to tumor growth dynamics and focus on brain tumors (glioma) because this type of tumor is one of the most vascularized (Zuelch 1986; Mikkelsen et al. 2003). We base our investigation on an experimental data set published by Lee et al. (2006). These data correspond to in vivo tumor growth of implanted U87 glioma cells and the associated tumor-induced vascularization in nude mice brains. They provide a prototype brain tumor model that allows for measurements of the tumor progression and neovascular development that we will describe in more detail in the next section. We analyze the experimental data by applying and extending a mathematical model of tumor growth considered by Cristini et al. (2003) and address in particular the following questions:

- What is the critical tumor size at which angiogenesis is initiated?
- What is the interplay between vascularization dynamics and glioma growth?
- Why does the tumor radius seem to grow linearly with time (Brù et al. 2003), at later stages of growth, and what are the corresponding consequences?

Even though each of these questions may have been addressed independently in former studies (see below for a short review of tumor-induced angiogenesis models), we will provide a unified approach to answer these questions and explain the connections between them. As an outlook, we will underline what are the implications of our findings in the context of anti-angiogenic treatment and how this may affect the post-treatment tumor dynamics.

There is a rich literature on mathematical modeling of tumor-induced vascularization and angiogenesis. A large part of the literature focuses on the spatio-temporal dynamics of vessel formation and the morphology of the resulting vasculature (e.g., Stokes et al. 1991; Anderson and Chaplain 1998; Plank and Sleeman 2003; Sun et al. 2005; Kevrekidis et al. 2006; Bauer et al. 2007; Milde et al. 2008). The coupling of blood flow and network remodeling has also been studied by various authors (e.g., Pries et al. 1998; McDougall et al. 2002; Stephanou et al. 2005; McDougall et al. 2006; Stephanou et al. 2006; Wu et al. 2007; Zhao et al. 2007; Pries and Secomb 2008; Sun and Munn 2008). Merks and Glazier (2006) describe the initial stage of angiogenesis, which requires the so-called sprouting instability. Vasculogenesis, i.e., de novo formation of vascular networks, has also been studied in Merks et al. (2008) and a review of older papers can be found in Ambrosi et al. (2005).

The first model that (nonlinearly) couples tumor growth and angiogenesis was developed by Zheng et al. (2005). Other more recent models of coupling between vascularization and tumor growth can be found in Frieboes et al. (2007); Welter et al. (2008); Bearer et al. (2009); Macklin et al. (2009); Welter and Rieger (2010). The connection of our work to the earlier papers is that here we consider a simplified model that provides insight into the biophysical problem and help identify key parameters and growth regimes to be used for deeper investigations with more sophisticated models.

In this chapter, our starting point is a set of in vivo glioma mice data that we detail in Sect. 2. In Sect. 3, we briefly introduce the nonlinear mathematical model we use.

We calibrate the parameters of the model in Sect. 4 to reproduce the experimental data. As a result of this process, we gain new insight regarding the vascularization effects on tumor dynamics. Accordingly, we propose in Sect. 5 a scenario to explain the different growth regimes experimentally observed and we extend the original model to explore further this scenario in Sect. 6. We finally summarize our findings and discuss their implications in the context of therapeutical perspectives.

2 Description and Processing of Experimental Data

2.1 Observations of Glioma Xenografts in Mice

Animal models of cancer, including both traditional tumor transplant models and newer genetically engineered mouse models of cancer, have helped the investigation of tumor growth dynamics. Implantation of U87 MG glioma cells into immunodeficient animals produces solid intracerebral tumors where most of the growth characteristics of these tumors are reproducible. For such reasons, U87 MG is one of the most frequently used models for testing therapies for malignant gliomas. In this chapter, we use implanted xenografts of U87 MG in a nude mouse model in order to characterize tumor growth and vascular development of human glioma. We focus, in particular, on experimental data obtained by Lee et al. (2006).

In their study, Lee and coworkers investigated morphological and immunohistochemical features of glioma growth. Here, we mainly exploit the volumetric data of the growth. At eight distinct time points, the authors measured the tumor volume V (Fig. 10.1c) and the microvessel density MVD ρ_v (Fig. 10.1d), which accounts for the number of microvessels and endothelial cells within a given tumor area. MVD data are rarely quantitatively used as they do not contain conclusive information regarding vessel functionality. However, here we use MVD data together with tumor growth data to consider the relative number of endothelial and tumor cells, which displays an interesting and instructive nonmonotone behavior in time.

Immunohistochemical measurements were also performed for a more complete description of the growth of U87 MG intracranial xenografts and the host angiogenic response, which allowed the following observations. Eight hours after cell implantation, the cells were grouped together, and there was no evidence of modifications to surrounding host vessels. At this time, some of the implanted U87 MG cells proliferated actively. Twenty-four hours after cell implantation, the cells were still clustered together as a small mass, but with a center displaying signs of cell death. Discussions with the authors suggest that this may be an artifact resulting from the implantation technique rather than hypoxia induced central necrosis. This is a characteristic of these cell-lines that release vascular endothelial growth factors (VEGF) factors and triggers a fast and strong angiogenic response, avoiding therefore the occurrence of hypoxic regions and potentially resulting necrotic areas.

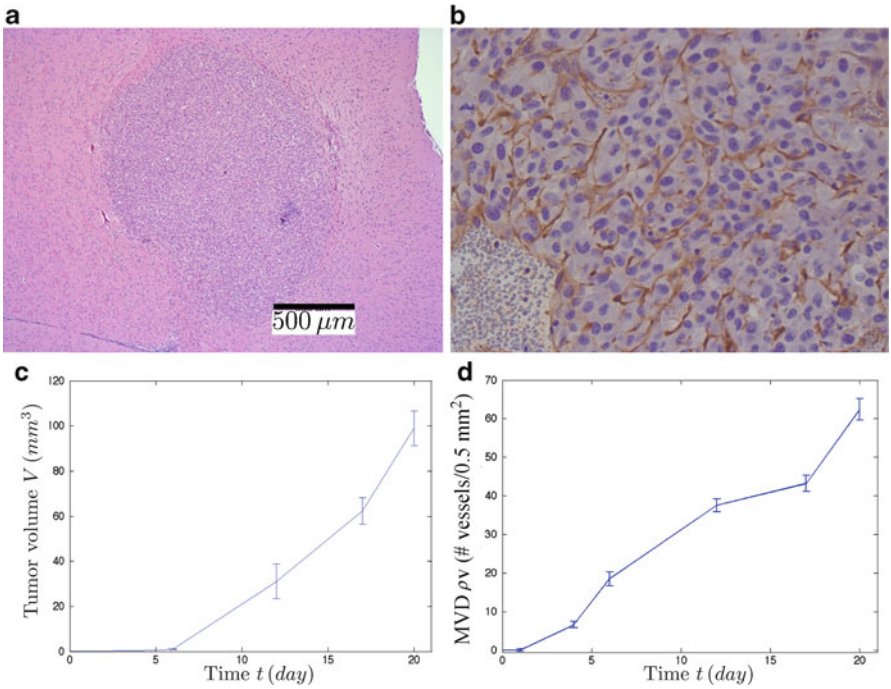

Fig. 10.1 (**a**) H&E staining of a human glioma xenograft U87 MG in a nude mouse model. Illustration of the spheroid morphology. (**b**) Spatial vessel distribution close to the tumor margin. (**c**) Temporal evolution of the experimental tumor volume. (**d**) Temporal evolution of the experimental mean vessel density

At the same time, vessels in the normal parenchyma of mice proximal to the tumor were observed. By Day 4, the tumors had grown to a mean volume $V = 0.37\text{mm}^3$ and contained a small area of dead cells surrounded by a mass of living tumor cells with a very low MVD. The vessels in the host parenchyma surrounding the tumor displayed changes in morphology, including an enlarged diameter and a disorganized structure. Some of the vessels interacted physically with peripheral tumor cells through the process of cooption and/or new branching. On Day 6 after implantation, although the tumors were small ($V \approx 1\text{mm}^3$), the MVD curve profile was within an exponential phase. Twelve days after implantation, the tumors were vascularized sphere-like masses of cells ($V = 31\text{mm}^3$) showing no signs of necrosis. The tumor margin was clearly defined and cancer cells did not exhibit an invasive pattern into host tissues. The tumor volume at Day 20 after implantation approximatively reached $V \approx 100\text{mm}^3$. At this time, the tumors also exhibited a high mean MVD plus a highly proliferative pattern without areas of necrosis. All mice showed signs of toxicity by Day 30, which correlates with the development of an expansive mass, causing extreme brain compression. The time-dependent volumetric characteristics are illustrated in Figs. 10.1c,d.

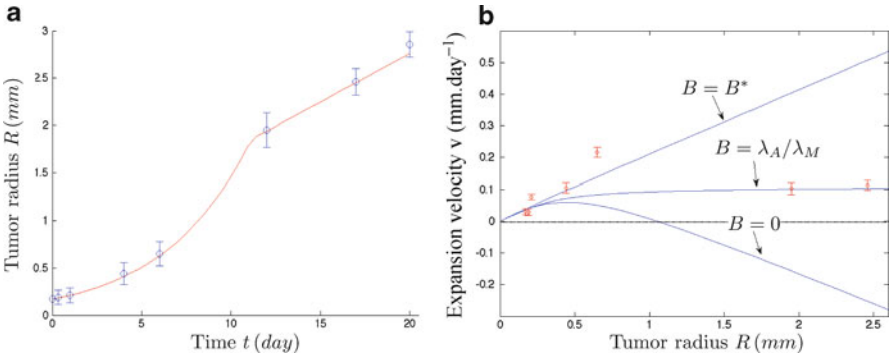

Fig. 10.2 (**a**) Temporal evolution of the tumor radius. The *circles* correspond to the experimental values obtained by data processing. The *solid line* corresponds to the best fit obtained from our model with B as a piecewise constant function of time (see text for details). (**b**) Regimes of tumor growth in the phase plan $(v(R), R)$. The *circles* correspond to the experimental values obtained by data processing. The three *solid curves* result from our model for different uniform values of B (see text for details)

2.2 Data Processing

We have processed the experimental observables of interest and especially the volumetric data. Indeed, the original data consists in the time evolution of the tumor mean volume $\mathbb{E}[V(t)]$ and the corresponding variance $\mathrm{Var}[V(t)]$. We work here under the assumption of radial symmetry, i.e., assuming that the tumor grows as a sphere, which is reasonable with respect to experimental observations (see Fig. 10.1a). We evaluate successively the mean value $\mu_R(t) = \mathbb{E}[R(t)]$ and the standard deviation $\sigma_R(t) = \sqrt{\mathrm{Var}[R(t)]}$ of the tumor radius $R(t)$, and $\mu_v(t) = \mathbb{E}[v(t)]$ and $\sigma_v(t) = \sqrt{\mathrm{Var}[v(t)]}$ of the growth speed $v(t)$, i.e., the time derivative of the tumor radius. The latest will help a better understanding of the growth regimes. The derivation of these quantities is presented in Appendix 1. We show our results in Figs. 10.2a,b.

3 Mathematical Modeling

We briefly introduce the mathematical model we use, which was originally published in Cristini et al. (2003). A more detailed description is provided in Appendix 2 at the end of this chapter. The model originally describes evolution of avascular and vascularized tumors but not the angiogenic transition between the two. Here, we show how to extend the model to describe the angiogenic transition.

The tumor is treated as an incompressible fluid flowing through a porous medium where tissue elasticity is simplified; the tumor–host interface is assumed to be sharp and cell-to-cell adhesive forces are modeled as a surface tension at the tumor–host

interface. The tumor expands as a mass whose growth is governed by a balance between cell birth (mitosis) and death (apoptosis, i.e., programmed cell-death). We focus on a description of nonnecrotic tumors because U87 MG xenografts show only few signs of necrosis during the development.

The mitotic rate within the tumor is assumed to be linearly dependent on the nutrient concentration and is therefore characterized by its maximal value λ_M at the tumor–host interface; we assume that the apoptosis rate λ_A is uniform. The concentration of nutrient obeys a reaction-diffusion equation in the tumor volume, where nutrient is supplied from the functional vasculature blood and consumed by the tumor cells at a uniform consumption rate.

The resulting dimensional problem can be reformulated into two nondimensional decoupled problems for modified variables, i.e., nutrient concentration and pressure within the tumor, respectively. From these problems, one can derive the following evolution equation for the full radius R of the tumor under the assumption that the tumor remains radially symmetric:

$$\frac{\mathrm{d}R}{\mathrm{d}t} = \frac{1}{3}(\lambda_M B - \lambda_A)R + \lambda_M(1-B)L_D\left(\frac{1}{\tanh(R/L_D)} - \frac{L_D}{R}\right), \qquad (10.1)$$

where the nonnegative parameter B represents the net effect of vascularization on the tumor radius evolution and L_D is an intrinsic length scale resulting from the nutrient dynamics, i.e., diffusion, supply, and consumption. This model has been shown in Cristini et al. (2003) to capture various growth regimes that are dictated by the values of the parameters λ_M, λ_A, and B, while the length scale L_D has been estimated in previous studies in the range $[0.1\mathrm{mm}, 0.2\mathrm{mm}]$ (see Ward and King 1997, for example). In particular, these regimes are:

1. *Low vascularization*: $B < \lambda_A/\lambda_M$.
   This regime includes the special case of avascular growth $B = 0$. Evolution is monotone and always leads to a stationary tumor spheroid.
2. *Moderate vascularization*: $\lambda_A/\lambda_M \leq B < 1$.
   Unbounded growth always occurs. The temporal growth of the spheroid radius tends to be exponential for $B > \lambda_A/\lambda_M$ and linear for $B = \lambda_A/\lambda_M$, respectively, at large radii.
3. *High vascularization*: $B \geq 1$.
   In this regime, both unbounded growth and total tumor shrinkage can be obtained, depending on the amount of apoptosis.

We will show in the next section how to calibrate the model parameters with respect to the experimental data from Lee et al. (2006).

4 Parameter Calibration

Our mathematical model predicts different growth regimes that can be better understood in terms of the velocity $v = \mathrm{d}R/\mathrm{d}t$ as a function of the radius R, i.e., the r.h.s. of (10.1). As previously explained, the tumor dynamics is controlled by

the value of B. We present in Fig. 10.2b three cases obtained after a first parameter exploration, together with the experimental velocities extracted from the data. The experimental data exhibit a rapid increase in tumor growth velocity at small radii. Then the velocity decreases to be approximately constant at large radii.

The lower curve is plotted by using $B = 0$ with particular values of λ_A and λ_M that will be later given. We observe that the maximum velocity value of this curve is far below the experimental maximum. This curve corresponds to the avascular case and can only reproduce the early phase of the growth. Indeed, the velocity starts decreasing after approximatively 12 h to reach a null value, which yields a steady spheroid where growth is stopped.

The intermediate curve corresponds to $B = \lambda_A/\lambda_M$, i.e., an asymptotically linear growth regime with constant speed, with the same previous values of λ_A and λ_M. For these values, the early growth phase is again captured by the model, while the late (linear) growth phase is now in excellent agreement with the experimental velocities. The intermediate phase is however poorly captured.

Keeping again the same values of λ_A and λ_M, the upper curve is plotted with $B = B^* > \lambda_A/\lambda_M$. We observe here that this case seems to better represent the intermediate growth phase.

These three examples, when compared to the experimental growth speed, suggests that different regimes occur during tumor growth. In particular, all the examples capture the initial phase, while $B = \lambda_A/\lambda_M$ reproduces the (linear) late phase and $B = B^*$ the intermediate one. We base the calibration of the parameters on this hypothesis and study in more detail each of these phases. We split the tumor growth in three different regimes: (1) early growth phase (Days 0–1 and radius smaller than 0.21mm), (2) transient growth phase (Days 1–12 and corresponding radii 0.21–1.95mm) and (3) late growth phase (Days 12–20 and corresponding radii 1.95–2.87mm).

4.1 Early Tumor Growth Phase (Days 0–1)

For a better understanding of the early growth predicted by our model, we work under the small radius assumption, i.e., we assume $R \ll L_D$ and develop the r.h.s. of (10.1) accordingly. We keep the two first orders and find the approximation

$$\frac{dR}{dt} \simeq \frac{1}{3}(\lambda_M - \lambda_A)R - \frac{\lambda_M(1-B)}{45L_D^2}R^3. \tag{10.2}$$

The first information we can extract is that the very early growth, dictated by the first term of the approximation, is always of exponential nature and does not depend on the parameter B (i.e., the tumor-induced vascularization effect). This first phase depends indeed solely on the net proliferation rate $\lambda_p^e = \lambda_M - \lambda_A$ at the early stage. By using the radius values at early times, we find $\lambda_p^e \approx 0.7\,\text{day}^{-1}$ which provides a good approximation of the experimental data.

The second observation is that the exponential growth is later affected by the vascularization through the parameter B, that starts playing a significant role when the two terms of the r.h.s. of (10.2) have similar orders of magnitude. This occurs around a critical radius R_c that can be evaluated by setting

$$\frac{1}{3}(\lambda_{\mathrm{M}} - \lambda_{\mathrm{A}})R_c \approx \frac{\lambda_{\mathrm{M}}(1-B)}{45L_{\mathrm{D}}^2}R_c^3. \tag{10.3}$$

As we have found $\lambda_{\mathrm{M}} - \lambda_{\mathrm{A}} = \lambda_p^e > 0$, which is necessary for initial growth, (10.3) requires $B < 1$, which is consistent with an initial low vascularization regime. Under this assumption, we evaluate

$$R_c \approx L_{\mathrm{D}}\sqrt{\frac{15(\lambda_{\mathrm{M}} - \lambda_{\mathrm{A}})}{\lambda_{\mathrm{M}}(1-B)}}. \tag{10.4}$$

This provides an estimate of the tumor size at which nonlinearities of the model, involving vascularization processes, start significantly influencing the initial exponential growth.

4.2 Late Tumor Growth Phase (Days 12–20)

From the experimental tumor velocity v at the late stages (see Fig. 10.2b), we assume here that the late tumor growth (after Day 12) evolves linearly, which is consistent with the long-term behavior of tumor growth where linear radial evolution is prominent (Brù et al. 2003). In our model, this assumption is equivalent to assigning $B = \lambda_{\mathrm{A}}/\lambda_{\mathrm{M}}$. For this value of B the (constant) asymptotic value v_∞ (i.e., $R \to \infty$ in (10.1)) of the velocity becomes

$$v_\infty = \left.\frac{\mathrm{d}R}{\mathrm{d}t}\right|_\infty = (\lambda_{\mathrm{M}} - \lambda_{\mathrm{A}})L_{\mathrm{D}}. \tag{10.5}$$

This phase then depends solely on the net proliferation rate $\lambda_p^l = \lambda_{\mathrm{M}} - \lambda_{\mathrm{A}}$ at the late stages, multiplied by the intrinsic length scale L_{D}. In order to minimize errors, we evaluate v_∞ by linearly fitting the experimental values of the radius using the three last time points (at Days 12, 17, and 20). We obtain the best fit using $\lambda_p^l L_{\mathrm{D}} \approx 0.11\,\mathrm{mm\,day^{-1}}$.

Assuming that the net proliferation $\lambda_p = \lambda_{\mathrm{M}} - \lambda_{\mathrm{A}}$ remains time-invariant, we can state that $\lambda_p^l = \lambda_p^e \approx 0.7\,\mathrm{day^{-1}}$, value extracted from the early exponential growth. This yields the value $L_{\mathrm{D}} \approx 0.16\,\mathrm{mm}$, which is consistent with previous studies that have shown that the nutrient diffusion length should be within the range $[0.1\mathrm{mm}, 0.2\mathrm{mm}]$.

To recapitulate, at this stage we have found the relation $\lambda_p = \lambda_M - \lambda_A \approx 0.7\,\text{day}^{-1}$ by focusing on the early phase of tumor growth, and the value $L_D \approx 0.16\,\text{mm}$ by focusing on the late phase. We have also observed that the early growth phase is independent of B, while the late one is accurately described by the particular value of $B = \lambda_A/\lambda_M$. If we assume time-invariant values of the characteristic mitotic rate λ_M and apoptosis rate λ_A and consider the plausible value $\lambda_M = 1\,\text{division}/18\,\text{h} \approx 1.3\,\text{day}^{-1}$, this yields $\lambda_A \approx 0.6\,\text{day}^{-1}$. Moreover, we have calculated an analytical estimate of the critical radius at which tumor-induced angiogenesis may initiate and affect the tumor growth through nonlinearities of our model. In the next section, we conclude the calibration by studying the intermediate growth phase.

4.3 Intermediate Tumor Growth Phase (Days 1–12)

During this transient regime, the growth dynamics is not obvious. As we have previously shown that the late regime is well described by using $B = \lambda_A/\lambda_M$ and that this value can also be taken for the early growth (independent of B), we first study the case of a time-invariant value of B, i.e., $B = \lambda_A/\lambda_M$ at any time of the growth. This yields a simplified version of (10.1) that becomes

$$\frac{dR}{dt} = \lambda_p L_D \left(\frac{1}{\tanh(R/L_D)} - \frac{L_D}{R} \right). \tag{10.6}$$

As we have already evaluated $\lambda_p \approx 0.7\,\text{day}^{-1}$ and $L_D \approx 0.16\,\text{mm}$, we present in Fig. 10.2b the corresponding curve of the velocity function of the radius. It is clear that our model cannot capture the dynamics of the tumor growth with B being constant during the tumor progression. This implies that a value $B^* > \lambda_A/\lambda_M$ is necessary during the intermediate regime of growth. We will use these values of λ_p and L_D together with the understanding of the various growth regimes provided by the parameter calibration to propose an insight into the global growth dynamics.

5 Likely Scenario for Tumor Growth Dynamics

Here, using the insight drawn from the previous section, we propose the most plausible scenario that describes the temporal evolution of the vascularization dynamics. The tumor initially follows an avascular exponential growth ($B = 0$). After the exponential phase and before the slowdown of the radial velocity, angiogenesis is triggered due to VEGF release by tumor cells, and a strong vascularization phase is initiated. The effective vasculature (functional vessels that allow for blood flow) matures, possibly supplying an excess of nutrients through blood flow with respect to the small size of the tumor. This regime has already been identified from

biologists and is characterized as an over-vascularization regime (Brown et al. 1997; Hlatky et al. 2002). This increased vascularization ($B = B^*$) places the tumor in a second exponential regime (slower than the first one) that takes over from the avascular growth (that would have ended up with a finite tumor size). Reaching finally its late stage, tumor growth relaxes to the linear regime ($B = \lambda_A/\lambda_M$) as an adaptation to the minimal requirement for unbounded growth.

We have previously shown that, by considering a time-invariant value of the parameter B in our model, we cannot reproduce the growth features experimentally observed. We propose here the simplest approach with the previously found time-invariant values of the characteristic mitotic rate λ_M and apoptosis rate λ_A and assume that B is a piecewise constant function of time. Each constant value of B is associated with one of the phases we have identified. This temporal variation may be seen as the result of vasculature changes triggered by angiogenesis, e.g., considering a dependence on the MVD ρ_v that is quickly increasing in time (see Fig. 10.1d). Under this assumption, we define B as follows:

- Early tumor growth (exponential regime): $B(t) = 0$ for $t \in [0, 1)$.
  As the early growth does not depend on B, the null value represents the most appropriate choice because no neovascularization is present at this time of the growth.
- Intermediate tumor growth (transient regime): $B(t) = B^* > \lambda_A/\lambda_M$ for $t \in [1, 12)$.
  This value can be seen as an average of B over the transient period because the exact modulation of B cannot be determined by the small number of measurement points.
- Late tumor growth (linear regime): $B(t) = \lambda_A/\lambda_M$ for $t \in [12, 20]$.
  According to the values $\lambda_M \approx 1.3\,\text{day}^{-1}$ and $\lambda_A \approx 0.6\,\text{day}^{-1}$, we find that $B \approx 0.46$ during this phase.

Our parameter exploration yielded the value $B^* \approx 0.9$ that puts the intermediate phase still in a moderate vascularization regime because $B^* < 1$. We show the corresponding simulation result on Fig. 10.2a, which is in excellent agreement with the experimental data.

Our approach, defining B as a piecewise constant function of time, is obviously a model simplification. A more likely scenario using a continuous function $B(t)$ is sketched in Fig. 10.3a, which shows the correlation between tumor growth and vascularization as the result of our data-driven analysis.

An interesting question that arises is how to link the overshooting of B with the experimental data. One piece of the experimental data we have not used so far is the microvessel density MVD ρ_v. It is the only available experimental measurement that could inform us on the evolution of the vasculature. However, it has been shown in the literature that MVD provides only limited information concerning angiogenic and tumor dynamics. In particular, Hlatky et al. (2002) critically discussed the usefulness of MVD and have concluded that MVD mainly contributes as a prognostic indicator, in the sense of metastatic likelihood and assessment of the current stage of the disease. These authors claim that the MVD by itself cannot

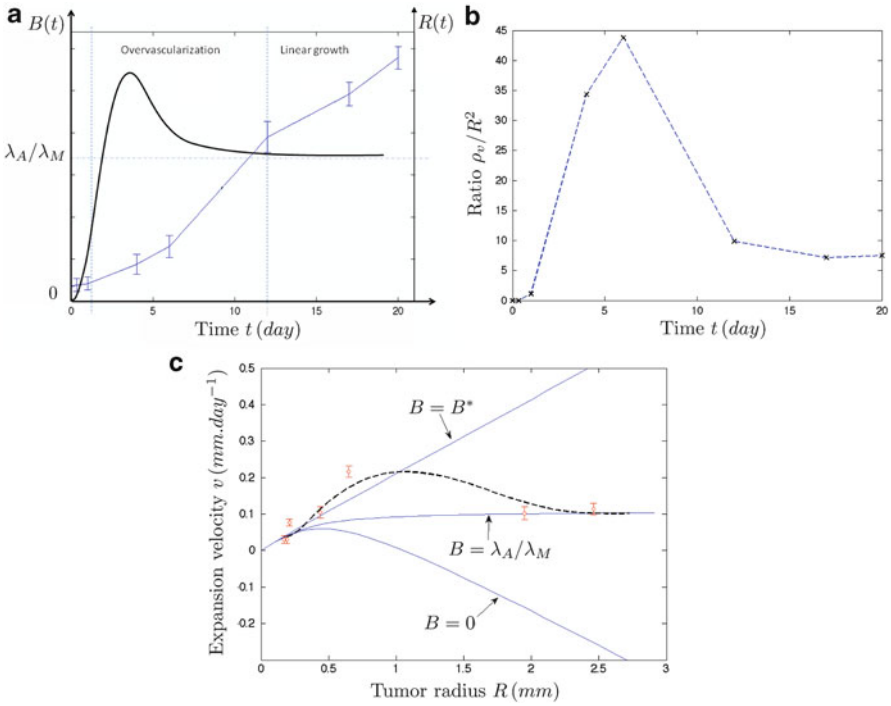

Fig. 10.3 (**a**) Likely scenario of the time-dependent coupling between the vascularization parameter B and the tumor growth regimes (this graph is no simulation result). The *bold curve* is an example of the time evolution of B that allows for the reproduction of the different tumor growth regimes experimentally observed and superimposed in the figure. (**b**) Temporal evolution of the ratio of vessel to tumor cell number $\rho_v(t)/R^2(t)$ evaluated from the experimental data. The nonmonotone behavior coincides with the time evolution of the parameter B. (**c**) Tumor radius velocity versus tumor radius: original model (*solid lines*); data of implanted U87 glioma in nude mice brains (*circles*); modified feedback-loop model (*dashed curve*, see text for details). The tumor dynamics predicted by the modified feedback-loop model is initially characterized by an exponential growth (where $B = 0$); then the velocity increases (due to overvascularization characterized by $B > \lambda_A/\lambda_M$) and reaches a maximum before decreasing and relaxing to a constant value, i.e., linear growth over time characterized by $B = \lambda_A/\lambda_M$

provide information about the dependence of tumor growth on angiogenic activity. However, the association of MDV with a parameter that expresses the influence of neovasculature on the tumor growth dynamics – in the context of our model – could provide another dimension to this measurement.

In the experimental setup used by Lee and coworkers, the MVD is evaluated as a number of vessels N_v^0 (including large microvessels and single brown-stained endothelial cells) within a surface $S_0 = 0.5\text{mm}^2$ in five different fields and averaged accordingly. The MVD is therefore experimentally evaluated as $\rho_v = N_v^0/S_0$ and is a monotonically increasing function of time (see Fig. 10.1d). As ρ_v is obtained as a spatial average, we can assume that the number of vessels N_v^0 within a constant

surface S entirely containing the tumor is $N_{\mathrm{v}}^0(t) = \rho_{\mathrm{v}}(t)S$. We evaluate now the number of tumor cells in S. They all are contained in a disc of radius R, which leads to a number of tumor cells $N_{\mathrm{T}}(t) = \rho_{\mathrm{T}}\pi R^2(t)$ in S, the tumor surface density ρ_{T} being constant. We build now the only dimensionless quantity extractable from the experimental measurement, i.e., the ratio of vessel to tumor cell number (or mass) in S, which yields

$$\frac{N_{\mathrm{v}}^0(t)}{N_{\mathrm{T}}(t)} = \frac{\rho_{\mathrm{v}}(t)S}{\rho_{\mathrm{T}}\pi R^2(t)} \propto \frac{\rho_{\mathrm{v}}(t)}{R^2(t)}. \tag{10.7}$$

Interestingly, this dimensionless quantity behaves in a similar manner to the parameter B, as depicted in Fig. 10.3b. It exhibits a local maximum in time as our predicted parameter B (Fig. 10.3a), and decreases relaxing further to a plateau. Therefore, we suggest that the dynamics of B may be associated with this ratio, which is supported by the scenario we have proposed: In a first stage, vascularization increases faster than the tumor. Then tumor growth accelerates, because supported by new vessels and additional nutrient supply. In the late stage, the number of necessary vessels equilibrates with the number of tumor cells to reach the minimal requirement for unbounded tumor growth.

6 Model Extension

Our data analysis and parameter calibration have provided a deeper insight in the interplay between tumor and vascularization dynamics. Of particular interest is the temporal evolution we have identified for the parameter B. We extend our original model to account for an intrinsic regulation of this parameter.

In tumor biology, angiogenic pathways, typically related to VEGF production, are activated to initiate angiogenic processes. In vivo secretion of VEGF is commonly assumed to depend on tumor hypoxia (Dvorak et al. 1995). VEGF affects endothelial cells of the existing vasculature, which further results in vessel instability, endothelial cell proliferation, and formation of a neovasculature whose vessels mature. When the neovascular network connects the tumor with the existing vasculature, tumor is perfused with blood that provides additional nutrient. This process eventually inhibits VEGF production, which reduces the formation of new capillaries.

In in vivo tumors, VEGFs are typically produced due to the activation of pathways related to reduced oxygen availability. In U87 tumors, histopathology data do not provide evidence of hypoxia. Indeed, U87 cells release VEGF "by default" even under normoxic conditions (Brown et al. 1997; Lucio-Eterovic et al. 2009). Therefore, we do not specify here any mechanism that up- and down-regulates VEGF release. However, due to the vascularization adaptation process (overshooting and relaxation) we believe there still exists a feedback loop between the tumor growth and the VEGF production. In particular, VEGF activation may be down-regulated either (1) by excessive oxygen supply from the new vessels or (2) by VEGF

diffusion through the capillaries. The above-described processes coincide with the definition of an activator–inhibitor system mediated by a negative feedback loop.

Accordingly, we extend our initial model to account for the coupling of VEGF and vascularization dynamics. We introduce the uniform VEGF concentration ρ_{VEGF} as a spatial average over the computational domain. A first-order ordinary differential equation (ODE) is used to model the temporal VEGF evolution. Concerning the dynamics of the vasculature effect B, the shape of the time evolution we have previously identified as a requirement to reproduce the evolution of the tumor radius over time (i.e., the overshooting regime) is typical of an excited damped oscillator. We write then the corresponding generic ODE system as follows:

$$\gamma_{\text{V}} \frac{\mathrm{d}\rho_{\text{VEGF}}}{\mathrm{d}t} + k_{\text{V}} \rho_{\text{VEGF}} = A_{\text{V}}(R,t) - I_{\text{V}}(B,R,t), \tag{10.8}$$

$$m_B \frac{\mathrm{d}^2 B}{\mathrm{d}t^2} + \gamma_B \frac{d\mathrm{B}}{\mathrm{d}t} + k_B B = A_B(\rho_{\text{VEGF}}, t). \tag{10.9}$$

In system (10.8)–(10.9), the coefficients γ_i, k_i (for $i = V, B$), and m_B are constant. Equation (10.8) models the evolution of the VEGF concentration: VEGF is produced through the activation term $A_{\text{V}}(R,t)$, diminished due to the vascularization effects through $I_{\text{V}}(B,R,t)$ and decays in time. The second equation (10.9) models the damped oscillating dynamics of B that is driven by the influence of VEGF concentration through $A_B(\rho_{\text{VEGF}}, t)$. VEGF signalling activates the formation of new vessels that requires several intermediate processes (e.g., migration of endothelial cells toward the tumor, vessel maturation), which introduces a delay in the excitation of B. We account for this delay by using the second-order time derivative with "inertia" coefficient m_B, while γ_B is the "damping" coefficient. Finally, the parameter k_B models the "stiffness" (compliance) of the vascularization to any changes of the VEGF production. In our approach, tumor growth is still modeled by (10.1) with B now resulting from (10.9), while the tumor size (the radius R) can influence B through VEGF activation $A_{\text{V}}(R,t)$ and inhibition $I_{\text{V}}(B,R,t)$, respectively.

We aim here at testing if such an approach can capture the dynamics of B and simplify the new model as much as possible. To this end, we suppose that the coupling terms in (10.8) depend only on time and not on the tumor radius R: $A_{\text{V}}(R,t) \equiv c_R(t)$, $I_{\text{V}}(B,R,t) \equiv c_B B(t)$ and $A_B(\rho_{\text{VEGF}}, t) \equiv c_V \rho_{\text{VEGF}}(t)$ where c_B and c_V are constant, while $c_R(t)$ depends on time to reflect VEGF release over time by U87 cells. Indeed, the experimental data suggest that VEGF production by U87 cells is uncontrolled from the beginning of the experiment. This is due to genetic modifications of these cells, which allows them to secret VEGF right after the injection time. We assume that VEGF production factor $c_R(t)$ is initially high and then decreases and relaxes to a constant value at longer times. This can be justified by the fact that the U87 cells release large amount of VEGF from the very beginning of their implantation. The system of (10.8)–(10.9) is decoupled from the tumor evolution although the function $B(t)$ influences the tumor growth through (10.1).

Solving the system of (10.8)–(10.9) and (10.1) and tuning accordingly the parameters, we calculate a potential trajectory of the system in the phase space. We observe that the simulated tumor velocity $v(R)$, the dashed curve in Fig. 10.3c, follows a trajectory similar to the one derived from the experimental observations. In particular, the tumor velocity overshoots and then relaxes to a constant value, recovering the linear growth regime at longer times. Therefore, we conclude that by assuming a feedback mechanism between VEGF release and effective vasculature, we can explain the overvascularization regime and the linear evolution of the tumor radius as a result of an adaptation process between the metabolic needs of the tumor and the vascularization dynamics.

7 Summary and Discussion

In this chapter, we have studied the coupling between tumor growth and tumor-induced neovascularization using a mathematical model informed by data obtained from U87 tumors grown in the brain of immunodeficient mice. Driven by the data analysis, we have used the mathematical model to reproduce the experimental volumetric data. Through this process, we have gained a better understanding of the tumor dynamics to answer the following questions.

What is the critical tumor size where angiogenesis is initiated?

Our model shows that the initial phase of tumor growth is of exponential nature and does not depend on vascularization, i.e., the evolution of the tumor radius is described by the leading term of (10.2):

$$\frac{\mathrm{d}R}{\mathrm{d}t} = \frac{1}{3}(\lambda_{\mathrm{M}} - \lambda_{\mathrm{A}})R\,.$$

This means that there exists a critical radius R_c (hence a critical time) until which angiogenesis – and eventually vascularization represented by the parameter B – confers no evolutionary advantage to tumor growth. We have derived the following expression for this critical radius:

$$R_c \approx L_{\mathrm{D}}\sqrt{\frac{15(\lambda_{\mathrm{M}} - \lambda_{\mathrm{A}})}{\lambda_{\mathrm{M}}(1-B)}}.$$

The above relation provides an approximate tumor radius where the nonlinearities (involving B) of (10.2) become significant. The effect of the nonlinear terms is to saturate the growth, i.e., $\mathrm{d}R/\mathrm{d}t = 0$ when the radius reaches R_c. As only exponential growth is observed for small radii (early phase), we argue that angiogenesis should be activated before the critical tumor radius and suggest that R_c is an upper bound for the development of angiogenic processes.

We can therefore predict the value of the avascular tumor critical radius R_c when knowing the value of the parameters present in the earlier expression. During the parameter calibration, we have found $\lambda_M \approx 1.3\,\text{day}^{-1}$, $\lambda_A \approx 0.6\,\text{day}^{-1}$, and $L_D \approx 0.16\,\text{mm}$. By assuming that the tumor is completely avascular in that early phase, i.e., $B = 0$, we can evaluate the corresponding value $R_c \approx 0.45\,\text{mm}$. This value of the critical radius is in excellent agreement with the experimental observations, since Lee et al. (2006) localize the end of the avascular phase around the first day where the tumor radius is 0.44 mm.

What is the interplay between vascularization dynamics and glioma growth?

The parameter calibration for our mathematical model has revealed further details of the interplay between vascularization and tumor growth dynamics. In particular, we have concluded in a biologically plausible scenario for the temporal evolution of the tumor dynamics (Fig. 10.3a). We claim, with the support of the data, that the tumor initially follows an exponential growth. During this avascular phase, U87 tumor cells initiate angiogenic processes (VEGF release), which results in the formation of a neovasculature. Follows then a highly vascularized phase that places the tumor in an overvascularization regime with an excess of new vessels and, potentially, an increase of blood flow. The increased vascularization boosts the tumor into a second exponential regime (however slower than the first one) that takes over from the avascular growth (that would have ended up in a steady tumor size). Reaching finally its late phase, tumor growth relaxes to a linear regime where the vasculature adapts to the metabolic needs of the tumor (see also next question).

Driven by these results, we have proposed an extension of our initial model to take into account a feedback mechanism between VEGF production and tumor vascularization. We have shown that the modified model, incorporating this self-regulated mechanism, was also capable of reproducing the earlier discussed vascularization and tumor growth dynamics.

Why does linear growth regime occur at the latest phase?

An aspect of interest in tumor growth dynamics is the linear expansion regime. As previously stated, linear growth seems to be a common feature to in vivo human and animal tumors (Brù et al. 2003). The experimental measurements by Lee and coworkers led us to the conclusion that, after a transient regime, the late growth we observe in this model of glioma is also linear. In our model, linear growth is asymptotically realized for the only particular value $B = \lambda_A/\lambda_M$, i.e., when proliferation weighted by vascularization balances cell death. This means that the tumor, in order to sustain unbounded growth, compensates cell death by increasing the tumor cell proliferation rate (which is proportional to the nutrient supply) by means of neovascularization.

At this point, the linear growth regime could be seen as a manifestation of spatio-temporal homeorhesis (*Greek:* stable flow). In biology is well established the concept of homeostasis, that is the tendency of living organisms to maintain (or return to) a stable steady state among its interacting internal components, regardless of the interactions with the external environment. Homeorhesis is a dynamical generalization of homeostasis describing a system that returns to a steady evolution trajectory (*chreod*) under internal and external disturbances (Waddington 1957). Biologically, it can be interpreted as the natural tendency of living organisms to continue their development, albeit being possibly different under different environmental conditions. Therefore, we suggest that tumors sustain a linear growth by returning always to a trajectory of expansion that is defined as the equilibration of the vascularization and metabolism dynamics. Moreover, linear tumor growth can be viewed as a solution to a minimization process of the energy expenditures for creating sufficient new vasculature, i.e., minimal value of B, in order to sustain a constant linear expansion rate.

Anti-angiogenic therapeutical implications and Outlook

Here, we comment on the implications of our study to the use of anti-angiogenic therapies against tumor growth. Our model suggests an explanation for the often disappointing efficacy of anti-angiogenic therapy observed in human clinical trials. Acknowledging the fact that anti-angiogenic treatments aim at depriving the tumor of nutrient through the inhibition of neovascularization processes, we show that a tumor cannot be eradicated (i.e., $R = 0$) by means of nutrient deprivation. This can be understood from the solution of (10.1): if a treatment (modeled by setting $B = 0$) is administrated at the late phase of the growth (at large radii), the tumor radius would initially decrease due to diminished nutrient supply, but would eventually stabilize at a finite size (intersection of the $B = 0$ orbit with the R-axis in Fig. 10.2b).

As stated earlier, the introduction of anti-angiogenic therapy in our model would imply a reduction of the vascularization parameter B. In Cristini et al. (2003) it has been shown that lowering B below a critical value may also affect the tumor morphology. In particular, for low enough values of B the tumor boundary becomes unstable and its morphology deviates from the spherical one. The resulting "fingering" morphology corresponds to in vivo observed tumor invasive patterns (see also Frieboes et al. 2007). The emergence of an invasive tumor cell phenotype would imply that tumor cells tend to "diffuse" away from the tumor bulk to reach better nourished locations, which allows for the creation of new tumor colonies. Therefore, the initiation of tumor invasion, due to treatment-induced hypoxia, could also reduce the efficacy of anti-angiogenic therapy.

Finally, we have shown that a feedback loop between VEGF release and vascularization effect could explain the adaptive behavior of the vascularization dynamics. A straightforward extension of our approach is to consider hypoxia as the cause of VEGF release, thus assuming that low oxygen concentration activates the vascularization dynamics. The neovasculature would increase oxygen supply to the

tumor, i.e., relax the hypoxic conditions, resulting in the inhibition of angiogenic signals. Including this mechanism in the current formulation of our model would improve the description of the biology of in vivo tumors. Assuming that anti-angiogenic treatment inhibits the vascularization effect through B, we could use this model as a basis for optimization of anti-angiogenic therapy protocols.

Acknowledgements HH, AC, and VC acknowledge support from The Cullen Trust for Health Care and the National Institute for Health, Integrative Cancer Biology Program: 1U54CA149196, for the Center for Systematic Modeling of Cancer Development. JL and VC acknowledge support from the National Science Foundation, Division of Mathematical Sciences. VC also acknowledges support from the National Cancer Institute. H. Hatzikirou and A. Chauvière contributed equally to this work.

Appendix 1. Data Processing

We present here the detailed derivation of the results of Sect. 2.2. We start with evaluating the temporal evolution of the tumor radius under the assumption of radial symmetry. We assume that the radii $R(t)$ are random variables (r.v.) – as biological observations include a degree of stochasticity – following the normal distribution $\mathcal{N}(\mu_R(t), \sigma_R(t))$ where $\mu_R(t) = \mathbb{E}[R(t)]$ and $\sigma_R(t) = \sqrt{\text{Var}[R(t)]}$ are the mean value and the standard deviation of $R(t)$, respectively. Therefore, we can assume that the r.v. $\{R(t)\}_{t\in T}$, where T the time of the process (in our case, a discrete time set), are subjected to Gaussian Markov process.[1] As the volume of the tumor is given by

$$V(t) = \frac{4\pi}{3} R^3(t),$$

it is proportional to the third raw moment of the radius. Therefore, we can explicitly write down, at each time point, the relations between the first two central moments (mean and variance) of the volume and the radius. For the sake of simplicity, we drop the time argument to write

$$\mathbb{E}[V] = \mathbb{E}\left[\frac{4\pi}{3} R^3\right] = \frac{4\pi}{3} \int_{\mathbb{R}} r^3 f(r) \mathrm{d}r = \frac{4\pi}{3} \left(\mu_R^2 + 3\mu_R \sigma_R^2\right), \quad (10.10)$$

$$\begin{aligned} \text{Var}[V] &= \mathbb{E}[V^2] - \mathbb{E}[V]^2 = \frac{4\pi}{3} \left[\int_{\mathbb{R}} r^6 f(r) \mathrm{d}r - \left(\int_{\mathbb{R}} r^3 f(r) \mathrm{d}r\right)^2\right] \\ &= 20\pi\sigma_R^2 \left(\mu_R^4 + \frac{36}{15}\mu_R^2 + 1\right), \end{aligned} \quad (10.11)$$

[1] A Gaussian Markov process $X(t)$ is a Markov process whose probability density function is Gaussian.

where $f(r) = \exp\left(-\frac{1}{2}(r-\mu_R)^2/\sigma_R^2\right)$ is the probability density function of the normal distribution. The solution of system (10.10)–(10.11) provides us with the mean μ_R and variance σ_R of the radius R at each time point of the experiment.

A more challenging task is the calculation of the tumor expansion rate (the tumor speed $v(t) = \mathrm{d}R(t)/\mathrm{d}t$), i.e., the radius increase per unit of time. Our approach consists in writing the process that dictates the radius evolution as the stochastic differential equation

$$\mathrm{d}R(t) = M(R,t)\mathrm{d}t + \Sigma(R,t)\mathrm{d}W(t), \tag{10.12}$$

where $M(R,t) = \mu_v(t)$ and $\Sigma^2(R,t) = \sigma_v^2(t) + \mu_v^2(t)$. In particular, the quantity $M(R,t)$, which is called drift, denotes the first moment of the velocity

$$M(R,t) = \lim_{\tau\to 0} \frac{\mathbb{E}[R(t+\tau) - R(t)]}{\tau} = \lim_{\tau\to 0} \frac{\mu_R(t+\tau) - \mu_R(t)}{\tau}, \tag{10.13}$$

where τ is an infinitesimal time step. The quantity $\Sigma(R,t)$, so-called diffusion coefficient, corresponds to the second moment of the velocity, i.e.,

$$\Sigma^2(R,t) = \lim_{\tau\to 0} \frac{\mathbb{E}[(R(t+\tau) - R(t))^2]}{\tau}. \tag{10.14}$$

According to the stochastic differential equations theory, the noise $W(t)$ corresponds to Wiener processes for each time point and $W(t) \sim \mathcal{N}(0,1)$ (property of the Gaussian processes).

Equation (10.14) can be reformulated by using $\mathbb{E}[A+B] = \mathbb{E}[A] + \mathbb{E}[B]$ as

$$\Sigma^2(R,t) = \lim_{\tau\to 0} \frac{1}{\tau}\Big(\mathbb{E}[R^2(t+\tau)] + \mathbb{E}[R^2(t)] - 2\mathbb{E}[R(t+\tau)R(t)]\Big). \tag{10.15}$$

In (10.15), the second moment of $R(t)$ corresponds to $\mathbb{E}[R^2(t)] = \sigma_R^2(t) + \mu_R^2(t)$ for any time t. The quantity $\mathbb{E}[R(t+\tau)R(t)]$ is the autocorrelation function of the process that quantifies how much correlated are two radii at successive times t and $t+\tau$. Under the assumption of a stationary Markovian process (i.e., assuming that the calculation of $R(t+\tau)$ requires only the knowledge of $R(t)$ with the corresponding transition probability being time invariant) the autocorrelation function rewrites

$$\begin{aligned}\mathbb{E}[R(t+\tau)R(t)] &= \sigma_R^2(t)e^{-\beta\tau} + \mathbb{E}[R(t+\tau)]\mathbb{E}[R(t)] \\ &= \sigma_R^2(t)e^{-\beta\tau} + \mu_R(t+\tau)\mu_R(t),\end{aligned} \tag{10.16}$$

where β is the characteristic relaxation rate of the autocorrelation function.

As the experimental observations correspond to a discrete time process $T = \{t_1, ..., t_n\}$, $n = 8$ being the number of experimental measurements, we use the discrete version of the (10.12)

$$R(t_i + \tau_i) - R(t_i) = M(R,t_i)\tau_i + \Sigma(R,t_i)\Delta W(t_i)\sqrt{\tau_i}. \tag{10.17}$$

In (10.17), the set $\{\tau_i\}_{i=1...n-1}$ corresponds to the time intervals between the experimental observations and the noises $\Delta W(t_i) \sim \mathcal{N}(0,1)$ are identically, normally distributed. We use the following discrete form of the stochastic drift:

$$M(R,t_i) \equiv \mu_v(t_i) = \frac{\mu_R(t_i+\tau_i)-\mu_R(t_i)}{\tau_i}. \tag{10.18}$$

We assume that the time between two experimental observations is much larger than the process characteristic time, i.e., $\tau_i \gg 1/\beta$ for $i = 1...n-1$. This assumption corresponds to complete independence between two experimental measurements $R(t_i)$ and $R(t_i+\tau_i)$. Thanks to (10.16) we find $\mathbb{E}[R(t_i+\tau_i)R(t_i)] = \mu_R(t_i+\tau_i)\mu_R(t_i)$. Then the discrete form of the diffusion coefficient writes

$$\Sigma^2(R,t_i) = \frac{1}{\tau_i^2}\Big(\sigma_R^2(t_i+\tau_i)+\mu_R^2(t_i+\tau_i)+\sigma_R^2(t_i)+\mu_R^2(t_i)-2\mu_R(t_i+\tau_i)\mu_R(t_i)\Big), \tag{10.19}$$

which leads to

$$\sigma_v^2(t_i) = \mathrm{Var}[v(t)] = \Sigma^2(R,t_i) - M^2(R,t_i) = \frac{\sigma_R^2(t_i+\tau_i)+\sigma_R^2(t_i)}{\tau_i^2}. \tag{10.20}$$

We can finally conclude that, at each time point t_i, the tumor velocity $v(t_i)$ can be evaluated through the normal distribution $\mathcal{N}\big(\mu_v(t_i),\sigma_v(t_i)\big)$ where μ_v and σ_v are given by (10.18) and (10.20), respectively.

Appendix 2. Details of the Mathematical Model

We consider a nonnecrotic tumor whose volume growth results from a balance between cell mitosis and cell apoptosis, driven by the presence of nutrient (e.g., oxygen or glucose). In the absence of inhibitor chemical species, the spatio-temporal dynamics of the nutrient concentration $\sigma(\mathbf{x},t)$ is modeled by the quasi-steady reaction-diffusion equation

$$0 = D\nabla^2\sigma + \Gamma, \tag{10.21}$$

where D is the diffusion coefficient and Γ is the rate at which nutrient is added to the tumor volume $\Omega(t)$. The quasi-steady assumption is well supported by the observation that the diffusion time scale for oxygen or glucose ($\sim$1 minute) is much lower than the cell doubling time ($\sim$1 day). The rate Γ incorporates all sources and sinks in the tumor volume and is based on the following phenomenological assumptions:

Biological assumption 1: Nutrient is homogeneously supplied by the vasculature at a rate $\Gamma_B = -\lambda_B(\sigma-\sigma_B)$ where σ_B is the uniform nutrient distribution in the blood and λ_B is uniform;

Biological assumption 2: Nutrient is consumed by tumor cells at a rate $\lambda\sigma$ with λ uniform.

This yields a rate Γ given by

$$\Gamma = -\lambda_B (\sigma - \sigma_B) - \lambda\sigma . \tag{10.22}$$

The tumor is modeled as an incompressible fluid whose velocity field $\mathbf{u}$ in Ω satisfies the continuity equation

$$\nabla \cdot \mathbf{u} = \lambda_{\mathrm{P}}, \tag{10.23}$$

where λ_{P} is the net proliferation rate that leads to volume growth (or decrease). This formulation rests on the additional assumptions:

Biological assumption 3: The tumor is modeled as a unique homogeneously distributed phenotype, meaning that all tumor cells behave in the same way;

Biological assumption 4: Tumor expansion depends solely on the net cell proliferation and invasive processes (e.g., cell diffusion) are not explicitly included;

Biological assumption 5: The model assumes that the density of tumor cells is constant and homogeneous within the tumor bulk.

The net cell proliferation rate is chosen as:

$$\lambda_{\mathrm{P}} = \lambda_{\mathrm{M}} \frac{\sigma}{\sigma^{\infty}} - \lambda_{\mathrm{A}}, \tag{10.24}$$

where σ^{∞} is the nutrient concentration outside the tumor volume and

Biological assumption 6: The mitotic and apoptotic rates λ_{M} and λ_{A} are uniform.

The velocity is assumed to obey Darcy's law (porous media flow)

$$\mathbf{u} = -\mu \nabla P, \tag{10.25}$$

where μ is a (constant) cell motility parameter and $P(\mathbf{x}, t)$ is the pressure inside the tumor that is assumed to satisfy the Laplace-Young boundary condition at the interface, which corresponds to

Biological assumption 7: Cell–cell adhesive forces are modeled by a surface tension γ at the tumor boundary.

By introducing the intrinsic length scale $L_{\mathrm{D}} = D^{1/2}/(\lambda_B + \lambda)^{1/2}$, we obtain an intrinsic relaxation time scale $\lambda_R^{-1} = (\mu\gamma)^{-1} L_{\mathrm{D}}^3$. We use these length and time scales to nondimensionalize our model that can be rewritten (using bar-notation for dimensionless quantities) in terms of the modified nutrient concentration $\bar{\sigma}$ and pressure $\bar{p}$ defined by:

$$\sigma = \sigma^{\infty}\big(1 - (1 - B)(1 - \bar{\sigma})\big),$$

$$P = \frac{\gamma}{L_{\mathrm{D}}} \left(\bar{p} + \frac{1}{\lambda_R} \left(\lambda_{\mathrm{M}}(1 - B)(1 - \bar{\sigma}) + (\lambda_{\mathrm{A}} - \lambda_M B) \frac{\bar{\boldsymbol{x}} \cdot \bar{\boldsymbol{x}}}{2d} \right) \right). \tag{10.26}$$

The parameter

$$B = \frac{\sigma_B}{\sigma^\infty}\frac{\lambda_B}{\lambda_B + \lambda} \tag{10.27}$$

represents the effect of vascularization. By using algebraic manipulations, the original dimensional problem can we reformulated in terms of two nondimensional decoupled problems:

$$\begin{aligned} \nabla^2\bar{\sigma} - \bar{\sigma} &= 0, \\ (\bar{\sigma})_\Sigma &= 1; \end{aligned} \tag{10.28}$$

and

$$\begin{aligned} \nabla^2\bar{p} &= 0, \\ (\bar{p})_\Sigma &= \kappa - \frac{1}{\lambda_R}(\lambda_\mathrm{A} - \lambda_M B)\frac{(\bar{\boldsymbol{x}}\cdot\bar{\boldsymbol{x}})_\Sigma}{2d}, \end{aligned} \tag{10.29}$$

in a d-dimensional tumor separated from the host tissue by the interface Σ (of local curvature κ) that evolves with the normal velocity $\bar{v} = \boldsymbol{n}\cdot(\bar{\boldsymbol{u}})_\Sigma$, $\boldsymbol{n}$ being the outward normal to Σ.

When considering evolution of a three-dimensional tumor that remains radially symmetric, problems (10.28) and (10.29) have analytical solutions that lead to the following evolution equation for the dimensionless tumor radius $\bar{R}$:

$$\frac{\mathrm{d}\bar{R}}{\mathrm{d}\bar{t}} = \bar{v} = \frac{1}{\lambda_R}\left(\frac{1}{3}(\lambda_\mathrm{M}B - \lambda_\mathrm{A})\bar{R} + \lambda_\mathrm{M}(1-B)\Big(\frac{1}{\tanh(\bar{R})} - \frac{1}{\bar{R}}\Big)\right). \tag{10.30}$$

We use the dimensional version of this equation for the tumor radius $R = L_\mathrm{D}\bar{R}$ evolving with respect to time $t = \bar{t}/\lambda_R$, which is (10.1) given in Sect. 3.

References

Ambrosi D, Bussolino F, Preziosi L (2005) A review of vasculogenesis models. Comp Math Meth Med 6:1–19

Anderson ARA, Chaplain MAJ (1998) Continuous and discrete mathematical models of tumor-induced angiogenesis. Bull Math Biol 60:857–900

Bauer AL, Jackson TL, Jiang Y (2007) A cell-based model exhibiting branching and anastomosis during tumor-induced angiogenesis. Biophys J 92:3105–3121

Bearer EL, Lowengrub JS, Chuang YL, Frieboes HB, Jin F, Wise SM, Ferrari M, Agus D, Cristini V (2009) Multiparameter computational modeling of tumor invasion. Canc Res 69(10):4493–4501

Brown LF, Detmar M, Claffey K, Nagy JA, Feng D, Dvorak AM, Dvorak HF (1997) Regulation of angiogenesis, Boston (MA): Birkhauser, chap Vascular permeability factor/vascular endothelial growth factor: a multifunctional angiogenic cytokine

Brù A, Albertos S, Subiza JL, Garcia-Asenjo JL, Bru I (2003) The universal dynamics of tumor growth. Bioph J 85:2948–2961

Cristini V, Lowengrub J, Nie Q (2003) Nonlinear simulation of tumor growth. J Math Biol 46:191–224

Dvorak HF, Brown LF, Detmar M, Dvorak AM (1995) Vascular permeability factor/vascular endothelial growth factor, microvascular hyperpermeability, and angiogenesis. Am J Pathol 146(5):1029–1039

Frieboes HB, Lowengrub JS, Wise S, Zheng X, Macklin P, Bearer E, Cristini V (2007) Computer simulation of glioma growth and morphology. NeuroImage 37:59–70

Hanahan D, Weinberg RA (2000) The hallmarks of cancer. Cell 100:57–70

Hlatky L, Hahnfeldt P, Folkman J (2002) Clinical application of antiangiogenic therapy: microvessel density, what it does and doesn't tell us. J Nat Canc Inst 94(12):883–893

Kevrekidis PG, Whitaker N, Good DJ, Herring GJ (2006) Minimal model for tumor angiogenesis. Phys Rev E 73:061,926

Lee O, Fueyo J, Xu J, Yung WK, Lemoine MG, Lang FF, Bekele BN, Zhou X, Alonso MA, Aldape KD, Fuller GN, Gomez-Manzano C (2006) Sustained angiopoietin-2 expression disrupts vessel formation and inhibits glioma growth. Neoplasia 8(5):419–428

Lucio-Eterovic AK, Piao Y, de Groot JF (2009) Mediators of glioblastoma resistance and invasion during antivascular endothelial growth factor therapy. Clin Cancer Res 15(14):4589–4599

Macklin P, McDougall S, Anderson ARA, Chaplain MAJ, Cristini V, Lowengrub J (2009) Multiscale modeling and nonlinear simulation of vascular tumour growth. J Math Biol 58(4-5):765–798

McDougall SR, Anderson ARA, Chaplain MAJ, Sherratt JA (2002) Mathematical modeling of flow through vascular networks: implications for tumour-induced angiogenesis and chemotherapy strategies. Bull Math Biol 64:673–702

McDougall SR, Anderson ARA, Chaplain MAJ (2006) Mathematical modeling of dynamic adaptive tumour-induced angiogenesis: Clinical applications and therapeutic targeting strategies. J Theor Biol 241:564–589

Merks RMH, Glazier JA (2006) Dynamic mechanisms of blood vessel growth. Nonlinearity 19:1–10

Merks RMH, Perrynand ED, Shirinifard A, Glazier JA (2008) Contact-inhibited chemotaxis in de-novo and sprouting blood-vessel growth. PLoS Comput Biol 4:e1000,163

Mikkelsen T, Enam SA, Rosenblum MR (2003) Invasion in malignant glioma, Philadelphia: W. B. Saunders Co., pp 687–713

Milde F, Bergdorf M, Koumoutsakos P (2008) A hybrid model for three-dimensional simulations of sprouting angiogenesis. Biophys J 95:3146–3160

Plank MJ, Sleeman BD (2003) A reinforced random walk model of tumour angiogenesis and anti-angiogenic strategies. Math Med Biol 20:135–181

Pries AR, Secomb TW (2008) Modeling structural adaptation of microcirculation. Microcirculation 15(8):753–764

Pries AR, Secomb TW, Gaehtgens P (1998) Structural adaptation and stability of microvascular networks: theory and simulations. Am J Physiol Heart Cir Physiol 275:349–360

Stephanou A, McDougall SR, Anderson ARA, Chaplain MAJ (2005) Mathematical modeling of flow in 2d and 3d vascular networks: Applications to anti-angiogenic and chemotherapeutic drug strategies. Math Comput Model 41:1137–1156

Stephanou A, McDougall SR, Anderson ARA, Chaplain MAJ (2006) Mathematical modeling of the influence of blood rheological properties upon adaptative tumour-induced angiogenesis. Math Comput Model 44:96–123

Stokes CL, Lauffenburger DA, Williams SK (1991) Migration of individual microvessel endothelial cells: stochastic model and parameter measurement. J Cell Sci 99(2):419–430

Sun C, Munn LL (2008) Lattice-boltzmann simulation of blood flow in digitized vessel networks. Comp Math Appl 55:1594–1600

Sun S, Wheeler MF, Obeyesekere M, Patrick CW Jr (2005) A deterministic model of growth factor-induced angiogenesis. Bull Math Biol 67:313–337

Waddington CH (1957) The Strategy of the Genes. Geo Allen & Unwin, London
Ward JP, King JR (1997) Mathematical modeling of avascular tumour growth. IMA J Math Appl Med Biol 14:36–69
Welter M, Rieger H (2010) Physical determinants of vascular network remodeling during tumor growth. Eur Phys J E Soft Matter 33:149–163
Welter M, Bartha K, Rieger H (2008) Emergent vascular network inhomogenities and resulting blood flow patterns in a growing tumor. J Theor Biol 250:257–280
Wu J, Xu SX, Long Q, Collins MW, Koenig CS, Zhao GP, Jiang YP, Padhani AR (2007) Simulation of microcirculation in solid tumors. In: IEEE/ICME Int. Conf. on Complex Med. Eng., pp 1555–1562
Zhao G, Wu J, Xu S, Collins MW, Long Q, Koenig CS, Jiang Y, Wang J, Padhani AR (2007) Numerical simulation of blood flow and interstitial fluid pressure in solid tumor microcirculation based on tumor-induced angiogenesis. Acta Mech Sinica 23:477–483
Zheng X, Wise SM, Cristini V (2005) Nonlinear simulation of tumor necrosis, neovascularization and tissue invasion via an adaptive finite-element/level-set method. Bull Math Biol 67:211–259
Zuelch KJ (1986) Brain tumors, 3rd edn. Heidelberg: Springer